



Construction of mesoporous carbon nitride/binary metal sulfide heterojunction photocatalysts for enhanced degradation of pollution under visible light



Qian Liang ^a, Jie Jin ^a, Miao Zhang ^a, Changhai Liu ^{c,*,**}, Song Xu ^a, Chao Yao ^a, Zhongyu Li ^{a,b,*}

^a School of Petrochemical Engineering, Changzhou University, Changzhou 213164, PR China

^b School of Environmental & Safety Engineering, Changzhou University, Changzhou 213164, PR China

^c School of Materials Science & Engineering, Jiangsu Collaborative Innovation Center of Photovoltaic Science and Engineering, Changzhou University, Changzhou 213164, PR China

ARTICLE INFO

Article history:

Received 4 May 2017

Received in revised form 28 June 2017

Accepted 1 July 2017

Available online 3 July 2017

Keywords:

Mesoporous graphitic carbon nitride

SnCoS_4

Heterojunction

Photocatalyst

ABSTRACT

A novel binary metal sulfide fabricated with mesoporous carbon nitride ($\text{mpg-C}_3\text{N}_4/\text{SnCoS}_4$) was synthesized by the simple *in situ* hydrothermal method. Characterizations indicate that a homogenous dispersion of SnCoS_4 nanoparticles on the ordered mesoporous structure of $\text{mpg-C}_3\text{N}_4$ ($248 \text{ m}^2 \text{ g}^{-1}$) with average diameter of 25 nm, providing more catalytic active sites and large contact regions for adsorption and degradation of pollutant. By taking advantage of this feature, the photocatalytic properties are evaluated systematically by degradation of rhodamine B (RhB) and methylene blue (MB) under visible light irradiation, and the photocatalytic performance of MCN/SnCoS_4-50 is much higher than that of pristine SnCoS_4 , $\text{mpg-C}_3\text{N}_4$, MCN/CoS_2 and MCN/SnS_2 . Moreover, $\text{mpg-C}_3\text{N}_4/\text{SnCoS}_4$ heterojunction exhibits excellent photostability after four recycles. The enhanced photo-induced oxidation and reduction activity of $\text{mpg-C}_3\text{N}_4/\text{SnCoS}_4$ can be attributed to not only the high surface area of composite, but also the formation of n-n type heterojunction. The incorporation of binary metal sulfides into $\text{mpg-C}_3\text{N}_4$ can decrease the band gap, alter the CB and VB potential, enhance the photoinduced interfacial charge transfer, and therefore increase the charge separation efficiency during the photocatalytic reaction.

© 2017 Elsevier B.V. All rights reserved.

1. Introduction

Semiconductor-based photocatalyst with its high efficiency and low cost offers a viable approach to solve environmental problems and energy crisis [1–3]. Metal sulfides, like SnS_2 and CoS_2 , are considered as one of the most widely studied semiconductors due to the relatively narrow band gap and valuable electronic property [4–6]. As 2D layered metal disulfide, SnS_2 with a band gap at about 1.9–2.3 eV has enhanced photocatalytic activity for organic pollutants degradation [7–9]. Recently, the binary metal sulfides ($\text{M}_x\text{N}_y\text{S}_z$) such as SnCoS_4 and $\text{Cd}_{0.5}\text{Zn}_{0.5}\text{S}$ have attracted much attention, resulting from the formation of solid solution which can lead to the modification of the band gap and the absorption ability of visible light [10–12]. Ye et al. reported that SnCoS_4 exhib-

ited excellent photoelectric property in comparison with CoS_2 and SnS_2 [13], suggesting that SnCoS_4 had an extraordinary potential to decompose the organic pollutant under the visible light irradiation. However, similar to the SnS_2 or CoS_2 , SnCoS_4 is usually unstable as a photocatalyst because photocorrosion and high recombination rate of photogenerated electron-hole pairs limit its industrial application. Therefore, it is a great challenge to develop the binary metal sulfides based photocatalysts.

Graphitic carbon nitride ($\text{g-C}_3\text{N}_4$) as a typical metal-free semiconductor has attracted considerable attention for photocatalytic degradation [14], water splitting [15] and CO_2 reduction [16] due to low cost, stable chemical structure and strong visible-light absorption. The band-gap of $\text{g-C}_3\text{N}_4$ is about 2.7 eV and the CB level is relatively negative, facilitating the reduction ability of the photogenerated electrons [17–19]. However, the limited surface area and high recombination rate of photogenerated charge carriers restrict the photocatalytic performance of $\text{g-C}_3\text{N}_4$ [20,21]. In order to extend the spectral response of $\text{g-C}_3\text{N}_4$, many strategies including construction of composite systems and formation of porous nanostructure have been investigated [22–24]. In particular, meso-

* Corresponding author at: School of Petrochemical Engineering, Changzhou University, Changzhou 213164, PR China.

** Corresponding author.

E-mail addresses: liuch@cczu.edu.cn (C. Liu), [\(Z. Li\).](mailto:zhongyuli@mail.tsinghua.edu.cn)

porous $\text{g-C}_3\text{N}_4$ (mpg- C_3N_4) with facile templating methods could improve the surface area, control the morphology as well as pore diameter, and enhance the carrier mobility [25–27]. For example, Wang et al. prepared mpg- C_3N_4 by removal of SiO_2 template, promoting the photocatalytic activity of pristine $\text{g-C}_3\text{N}_4$ [28]. Suitable matching of the band gap between the two semiconductors can provide an efficient driving force to separate photogenerated electron-hole pairs [29]. Based on the purpose of constructing the efficient and stable photocatalyst, combining the property of mpg- C_3N_4 and binary metal sulfides to disperse of binary metal sulfides and broaden the spectral response is of vital importance. Nevertheless, less attention has been paid to the photocatalytic performance of mpg- C_3N_4 /binary metal sulfides.

Herein, a novel mpg- $\text{C}_3\text{N}_4/\text{SnCoS}_4$ heterojunction is synthesized via a facile *in situ* hydrothermal method. Rhodamine B (RhB) and methylene blue (MB) are chosen as the model pollutant to systematically evaluate the photocatalytic activity of as-prepared samples under visible-light irradiation. Compared to the mpg- $\text{C}_3\text{N}_4/\text{SnCoS}_4$, mpg- $\text{C}_3\text{N}_4/\text{CoS}_2$ and mpg- $\text{C}_3\text{N}_4/\text{SnS}_2$, the formed n-n type heterostructured photocatalyst of mpg- $\text{C}_3\text{N}_4/\text{SnCoS}_4$ exhibits high surface area, enhanced visible-light absorption range, narrow band gap, and significantly improved degradation efficiency of model pollutant, that shows not only an excellent degradation efficiency of MB (95%), but also good removal efficiency of RhB (70%). Besides, we have investigated the effect of different mpg- C_3N_4 content for the photocatalytic activity. The conduction band (CB) and valence band (VB) potentials as well as energy band gap of as-prepared samples were examined, and the trapping experiments are conducted to explain the photocatalytic mechanism. Finally, the charge transfer behavior between binary metal sulfide and mpg- C_3N_4 is also explored in detail.

2. Experimental

2.1. Synthesis of mpg- C_3N_4

SBA-15 was prepared by using P123 copolymer as a template. Typically, 2.0 g P123 was dissolved in 100 mL HCl aqueous solution (1.0 mol/L) under stirring, followed by adding 4.0 g tetraethyl orthosilicate. The mixture was stirred at 40 °C for 24 h, and then transferred into an autoclave and reacted at 130 °C for 24 h. After cooling to room temperature, the white precipitate was filtered and then calcined at 550 °C for 5 h to remove P123.

10 g dicyandiamide was dissolved into 30 mL of DMF under stirring, and then 1.0 g SBA-15 was added into the solution. After stirring for 6 h, the mixture was heated overnight in the oil bath, and the resultant solid was heated at 550 °C for 4 h with a heating rate of 2.3 °C/min under N_2 atmosphere. The brown powder was immersed in 100 mL NH_4HF_2 aqueous solution (4 mol/L) for 24 h to remove the SBA-15 template. The dispersion was filtered, washed and dried to obtain mpg- C_3N_4 .

2.2. Synthesis of mpg- $\text{C}_3\text{N}_4/\text{SnCoS}_4$

A mixture solution of 0.1136 g L-cysteine (0.9375 mmol), 0.0658 g $\text{SnCl}_4 \cdot 5\text{H}_2\text{O}$ (0.1875 mmol) and 0.0446 g $\text{CoCl}_4 \cdot 6\text{H}_2\text{O}$ (0.1875 mmol) in 20 mL deionized water was added dropwise into 20 mL suspension of mpg- C_3N_4 (0.2833 g). After stirring for 2 h, the mixture was transferred into a 100 mL Teflon-lined stainless steel autoclave and heated at 180 °C for 24 h. After cooling to room temperature, the black precipitate was collected by centrifugation, and washed with deionized water and ethanol for several times. The as-synthesized mpg- $\text{C}_3\text{N}_4/\text{SnCoS}_4$ composites were denoted as $\text{MCN}/\text{SnCoS}_4\text{-x}$, where x referred to the nominal weight ratios of SnCoS_4 to mpg- C_3N_4 that were 30% ($\text{MCN}/\text{SnCoS}_4\text{-30}$), 50%

($\text{MCN}/\text{SnCoS}_4\text{-50}$) and 100% ($\text{MCN}/\text{SnCoS}_4\text{-100}$). MCN/SnS_2 and MCN/CoS_2 samples were also prepared by the same hydrothermal method.

2.3. Characterization

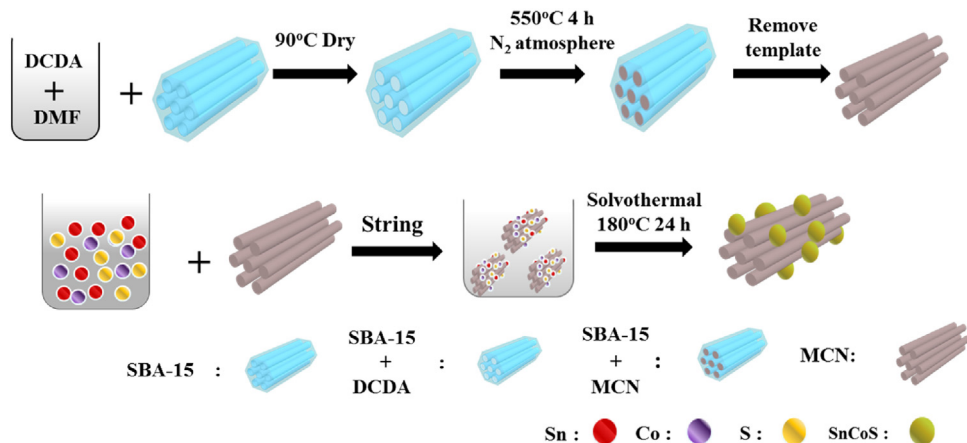
Powder X-ray diffraction (XRD) pattern was recorded by a Shimadzu XRD 6000 diffractometer using $\text{Cu K}\alpha$ ($\lambda = 0.15406 \text{ nm}$) radiation. The structure and morphology were observed by field emission scanning electron microscopy (FESEM) on a Quanta 200F instrument and transmission electron microscopy (TEM) on a JEOL JEM 2100 instrument. Fourier transform infrared spectroscopy (FT-IR) spectra were measured on an FTS-3000 spectrophotometer measured by using American Digilab Company. Specific surface area was obtained by adsorption-desorption of N_2 gas at 77 K equipped with a Micromeritics ASAP 2000 gas sorption analyzer. X-ray photoelectron spectra (XPS) were manufactured by a Perkin-Elmer PHI-1600 ESCA spectrometer via $\text{Mg K}\alpha$ ($\text{h}\nu = 1253.6 \text{ eV}$) X-ray source. TGA data were carried out using a Perker Elmer TGA6 instrument. Electron paramagnetic resonance (EPR) was obtained on a Bruker model A300 spectrometer. Raman spectra were performed on a laser with an excitation wavelength of 532 nm at room temperature using a Thermo Scientific DXR Raman microscope. UV-vis diffused reflectance spectra (DRS) were obtained on a UV-vis spectrophotometer (Hitachi U-4100). Steady state photoluminescence (PL) spectra were measured by a Cary Eclipse fluorescence spectrophotometer.

2.4. Evaluation of the photocatalytic activity

The photocatalytic degradation of organic pollutant with visible light irradiation was evaluated by using 300 W Xe arc lamp equipped with an UV cut-off filter ($\lambda \geq 420 \text{ nm}$). In a typical procedure, the as-prepared photocatalyst (20 mg) was mixed with the fresh aqueous solution of model pollutant (100 mL, 20 mg/L) under magnetically stirring for 30 min in the dark to achieve an adsorption-desorption equilibrium of model pollutant. During the experiment, ~2.0 mL the suspension was collected in a certain time interval. The clear solution was measured by the 759 UV-vis spectrophotometer after the photocatalyst was separated from the solution by centrifugation (4000 rpm for 15 min). To evaluate the photostability of the photocatalyst, the composite was collected by centrifugation, and then the recovered photocatalyst was used for subsequent cycle test of photocatalytic degradation reaction with the same conditions. Furthermore, the photocatalytic mechanism was detected by species trapping. Benzoquinone (BQ), ethylenediaminetetraacetic acid disodium salt (EDTA-2Na) and isopropyl alcohol (IPA) were added to trap superoxide radical anions (O_2^-), holes (h^+) and hydroxyl radicals (•OH), respectively.

2.5. Electrochemical analysis

Mott-Schottky plots were measured on a CHI660D electrochemical analyzer via the Impedance-Potential mode. Measurements were evaluated using a conventional three-electrode cell including a Pt wire as counter electrode, a glass carbon (GC, $\Phi=3 \text{ mm}$) electrode as working electrode and an Ag/AgCl as reference electrode. The working electrode was used as the drop-coating method. Typically, the as-prepared sample (10 mg) was dispersed in absolute ethanol (5 mL) with an ultrasonic bath for 30 min. After that, the dispersion (5 μL) was dropped onto the GC electrode and dried at 50 °C for 3 h. The electrodes were immersed in 0.1 M Na_2SO_4 ($\text{pH}=5.6$) solution.



Scheme 1. Schematic illustration for the preparation of mpg- C_3N_4 /SnCoS₄ heterojunction.

3. Results and discussion

3.1. Characterization of morphology and structure

The mpg- C_3N_4 /SnCoS₄ was prepared by the two steps illustrated in **Scheme 1**: first step, the preparation of SBA-15-templated mpg- C_3N_4 with dicyandiamide (DCDA) as starting materials; second step, loading precursors into mpg- C_3N_4 to form SnCoS₄ within mesoporous frameworks. The morphology and particle size of the as-prepared samples were investigated by SEM (Fig. 1) and TEM (Fig. 2) images. From the SEM image in Fig. 1a, the pristine CoS₂ is consisted of aggregated spheroidal particles with homogeneous size and shape, while the bare SnS₂ appears as typical three-dimensional flower-like structure with an average diameter of 1.2 μm (Fig. 1b). The surface morphology of synthesized SnCoS₄ displays smaller spherical aggregated particles (Fig. 1c), and that of mpg- C_3N_4 presents a multilayer stacking structure in Fig. S1. It can be clearly seen that after mpg- C_3N_4 is introduced, CoS₂ (Fig. 1d), SnS₂ (Fig. 1e), SnCoS₄ (Fig. 1f) with original morphology are uniformly anchored on the external surface of mpg- C_3N_4 . From the TEM image in Fig. 2a, mpg- C_3N_4 shows a linear array of ordered mesopores structure arranged in a regular pat-

tern, similar to the structure of SBA-15 template [30]. The CoS₂ nanoparticles with average diameter of 85 nm and SnS₂ nanoparticles with average diameter of 30 nm on the surface of mpg- C_3N_4 can be clearly observed. In comparison with mpg- C_3N_4 /CoS₂ and mpg- C_3N_4 /SnS₂, mpg- C_3N_4 /SnCoS₄ composite demonstrates more homogeneous nanoparticles with smaller average diameter of 25 nm. To corroborate the formation of heterojunction between mpg- C_3N_4 and SnCoS₄, HRTEM image is shown in Fig. 2e. The lattice spacings measured for the crystalline planes of SnCoS₄ are 0.32 nm [13], and the light parts without lattice spacings belong to mpg- C_3N_4 . The observed tight interface of heterojunction could be favorable for the photogenerated electron-hole pairs transfer between mpg- C_3N_4 and SnCoS₄. EDX analysis provides a direct evidence for determining the chemical composition, and EDX spectrum in Fig. 2f confirms the presence of Co, Sn and S elements in mpg- C_3N_4 /SnCoS₄ composite. The STEM image and EDX mapping of mpg- C_3N_4 /SnCoS₄ sample are shown in Fig. 2g. The white spots in the STEM image display a homogenous dispersion of SnCoS₄ nanoparticles composed of Co, Sn and S element, which is in good agreement with the result of the EDX spectrum.

Fig. 3a shows the XRD patterns of mpg- C_3N_4 , SnCoS₄ and mpg- C_3N_4 /SnCoS₄, and Fig. 3b reveals the XRD patterns of SnS₂, CoS₂

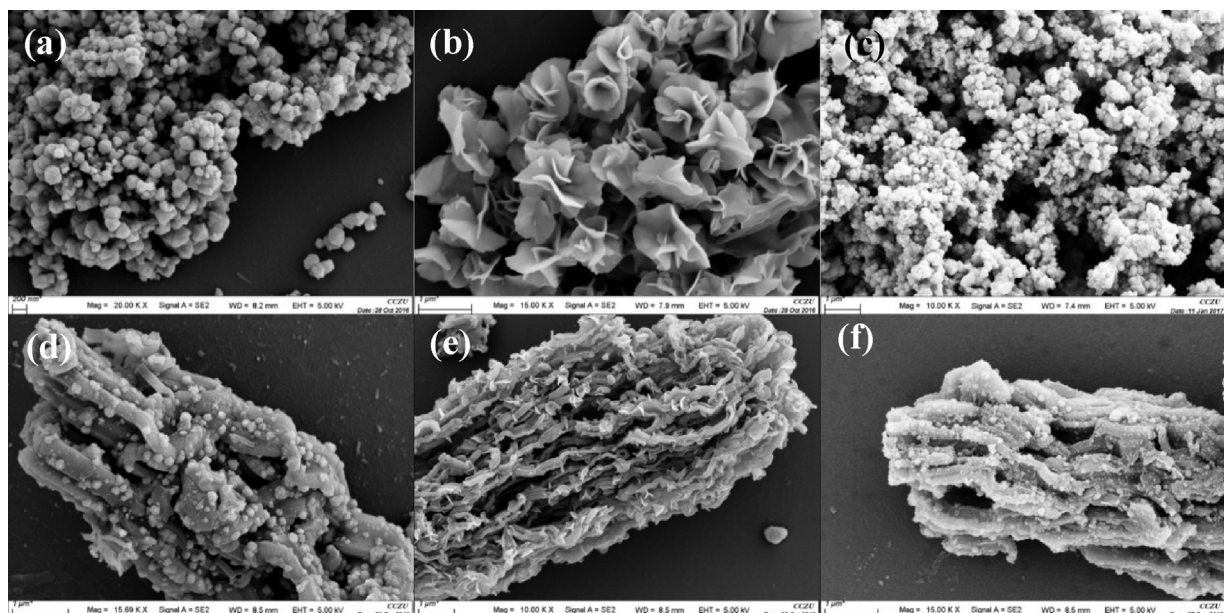


Fig. 1. SEM images of (a) CoS₂, (b) SnS₂, (c) SnCoS₄, (d) mpg- C_3N_4 /CoS₂, (e) mpg- C_3N_4 /SnS₂, (f) mpg- C_3N_4 /SnCoS₄.

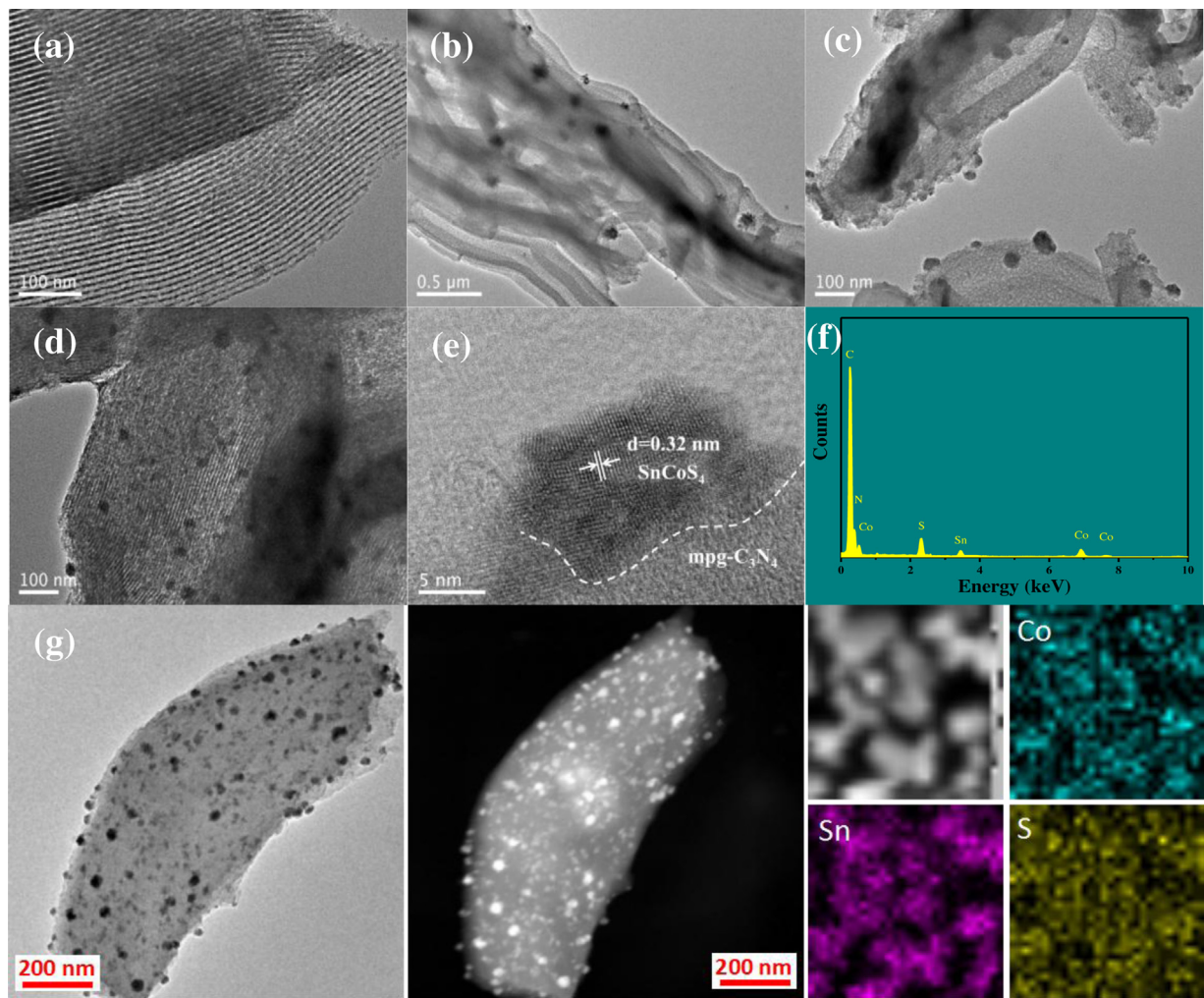


Fig. 2. TEM images of (a) mpg-C₃N₄, (b) mpg-C₃N₄/CoS₂, (c) mpg-C₃N₄/SnS₂, (d) mpg-C₃N₄/SnCoS₄, (e) HRTEM image of mpg-C₃N₄/SnCoS₄, (f) EDX pattern of mpg-C₃N₄/SnCoS₄, (g) EDX mapping of mpg-C₃N₄/SnCoS₄.

mpg-C₃N₄/SnS₂ and mpg-C₃N₄/CoS₂. The characteristic diffraction peaks of SnS₂ at 14.9°, 28.2°, 32.2°, 41.8° and 49.9° can be ascribed to hexagonal phase (JCPDS, No. 23-677) [31], corresponding to the major (001), (100), (101), (102) and (110) planes, while the characteristics peaks of CoS₂ at 27.9°, 32.3°, 36.3°, 39.9°, 46.3° and 55.2° are agreement with the standard cubic phase (JCPDS, No. 41-1471) [6]. The pristine SnCoS₄ exhibits the diffraction peaks at 28.7°, 32.2°, 51.1°, quite different from SnS₂ and CoS₂, demonstrating that the SnCoS₄ is a solid solution rather than a simple mixture of the SnS₂ and CoS₂ [13]. Besides, since the increased disorder and chemical inhomogeneity due to the smaller SnCoS₄ nanoparticle size, the pattern of SnCoS₄ shows a broad characteristic diffraction peaks. The mpg-C₃N₄/SnCoS₄ heterojunction shows the diffraction peaks of both mpg-C₃N₄ and SnCoS₄, indicating that the SnCoS₄ has been successfully loaded on mpg-C₃N₄ through the *in-situ* hydrothermal method. In addition, the spectrum of composite shows a large full width at half maximum (FWHM), suggesting that the mpg-C₃N₄ can effectively stabilize the small size of SnCoS₄ nanoparticles and prevent the nanoparticles from agglomerating, which is further confirmed by SEM and TEM images.

Fig. S3 shows the FT-IR spectra of the pure mpg-C₃N₄, SnCoS₄, mpg-C₃N₄/SnCoS₄, mpg-C₃N₄/CoS₂ and mpg-C₃N₄/SnS₂. For mpg-C₃N₄, all the characteristic FT-IR peaks assigned to typical g-C₃N₄ are observed. The strong peaks at 1200–1650 cm⁻¹ belong to the stretching vibrations of C–N heterocycles, while the peak at

807 cm⁻¹ is ascribed to the triazine units of g-C₃N₄ [32]. The broad peaks located at 3200–3500 cm⁻¹ are assignable to the adsorbed H₂O and N–H vibration. In the spectrum of mpg-C₃N₄/CoS₂, the main characteristic peaks around 1090 cm⁻¹ correspond to Co=S stretching vibration, while as the mpg-C₃N₄/SnS₂ sample, a broad band peaked at 550–600 cm⁻¹ is originated to the vibration of Sn–S bands [31]. For SnCoS₄ sample, the bands at 550–600, 778, 852, 1141, 1325 and 1635 cm⁻¹ are attributed to the characteristic peaks of SnCoS₄. The FT-IR spectrum of mpg-C₃N₄/SnCoS₄ represents the main characteristic peaks of SnCoS₄, especially the obvious Sn–S vibration mode at 550–600 cm⁻¹.

Fig. 4 shows the Raman spectra of mpg-C₃N₄, SnCoS₄ and mpg-C₃N₄/SnCoS₄. The characteristic peaks at 1348 and 1576 cm⁻¹ of mpg-C₃N₄ can be assigned to the D and G bands of graphitized carbon, respectively [33,34]. The Raman spectrum of SnCoS₄ exhibits the strong peaks at 820 and 994 cm⁻¹, while the Raman spectrum of mpg-C₃N₄/SnCoS₄ displays not only the characteristic peaks of SnCoS₄ at 820 and 994 cm⁻¹, but also the peaks of mpg-C₃N₄ at about 1348 and 1605 cm⁻¹, suggesting the formation of the composite structure. Furthermore, a blue shift of G band on the mpg-C₃N₄/SnCoS₄ from 1576 to 1605 cm⁻¹ can be observed, indicating that incorporation of SnCoS₄ has an effect on the sp² graphite carbon band of mpg-C₃N₄ [35], and further supporting the formation of heterojunction in the mpg-C₃N₄/SnCoS₄ composite.

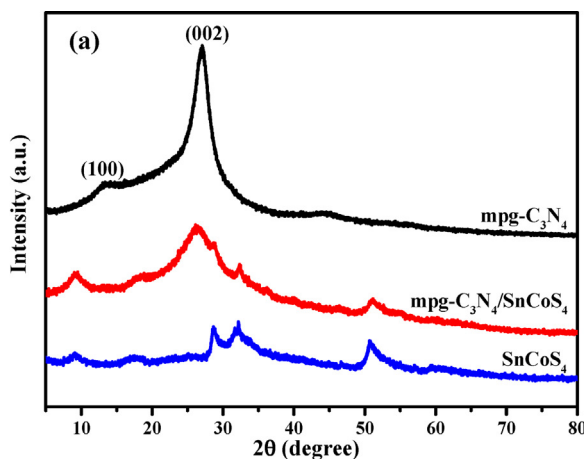


Fig. 3. XRD patterns of (a) mpg-C₃N₄, SnCoS₄ and mpg-C₃N₄/SnCoS₄, (b) SnS₂, CoS₂, mpg-C₃N₄/SnS₂ and mpg-C₃N₄/CoS₂.

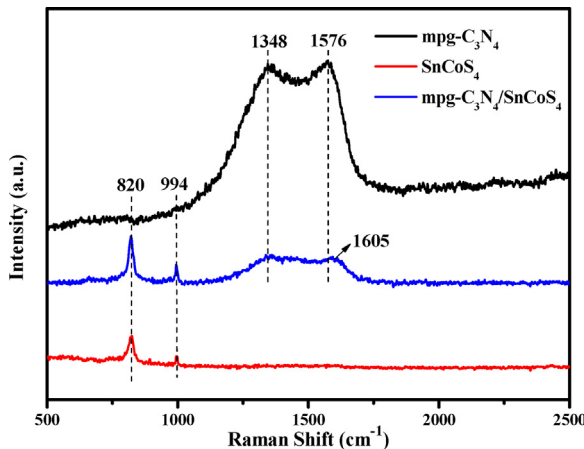


Fig. 4. Raman spectra of mpg-C₃N₄, SnCoS₄, mpg-C₃N₄/SnCoS₄.

In order to obtain more evidence to show the alternation of electronic band structure, EPR analysis is conducted to investigate the spin state of unpaired electrons as shown in Fig. 5. The mpg-C₃N₄ presents one single Lorentzian line with a similar factor of bulk g-C₃N₄, originating from the unpaired electrons in the π -bonded aromatic rings of carbon atoms [36]. What's more, the EPR intensity of mpg-C₃N₄/SnCoS₄ is greatly enhanced in comparison with pristine mpg-C₃N₄ and SnCoS₄. This result can be attributed to not only the more defect sites of SnCoS₄ due to the enlargement

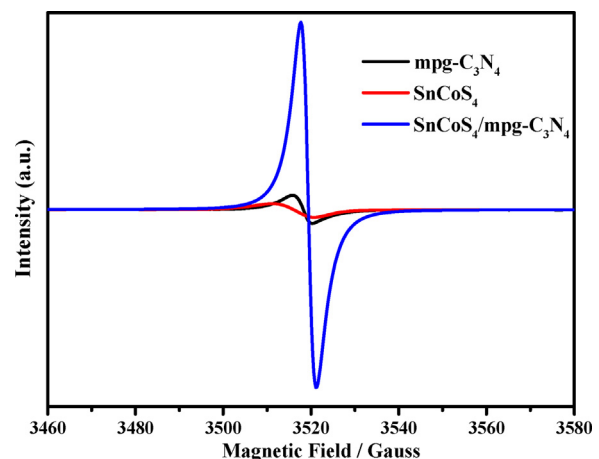


Fig. 5. EPR spectra of mpg-C₃N₄, SnCoS₄ and mpg-C₃N₄/SnCoS₄ at room temperature.

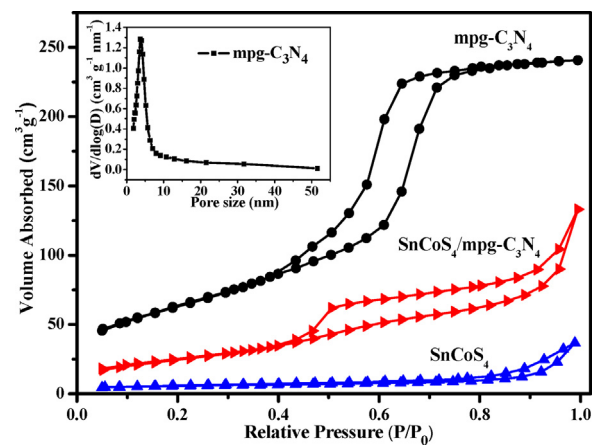


Fig. 6. Nitrogen adsorption-desorption isotherms of mpg-C₃N₄, SnCoS₄ and mpg-C₃N₄/SnCoS₄, and BJH pore-size distribution of mpg-C₃N₄ (inset).

of surface area, but also the more unpaired spin caused by heterostructure that can affect the π -conjugated system of g-C₃N₄ and promote exciton dissociation to obtain free electrons and holes for photocatalytic reaction [24].

N₂-adsorption/desorption isotherms of mpg-C₃N₄, SnCoS₄ and mpg-C₃N₄/SnCoS₄ are shown in Fig. 6. The pristine mpg-C₃N₄ has a BET surface area of 248 m² g⁻¹ and Langmuir surface area of 377 m² g⁻¹, and shows a typical type-IV isotherm with steep H1 hysteresis loop at 0.5–0.7 p/p₀, indicating the presence of ordered mesoporous structure [37]. Furthermore, the average pore size of mpg-C₃N₄ is about 4.5 nm, corresponding to the size of SBA-15 template. After introduction of SnCoS₄, the BET surface area and pore volume of mpg-C₃N₄/SnCoS₄ are decreased (Table S1) compared with pure mpg-C₃N₄, but the type of H1 hysteresis loop can be observed clearly, demonstrating that the SnCoS₄ nanoparticles are successfully embedded inside the mpg-C₃N₄ network and partially occupy its pore [38]. Although the surface area of composite is lower than that of mpg-C₃N₄, it is much higher than pristine SnCoS₄ and other binary metal sulfide-based materials, presenting that mpg-C₃N₄/SnCoS₄ can provide more surface active sites and make charge carrier transfer easier.

XPS is employed to determine the valence states of various species. The XPS survey spectrum of SnCoS₄ indicates the expected Sn, Co, S, O and C elements, while only the peaks of C, N and O appear in pure mpg-C₃N₄ as shown in Fig. 7a. In mpg-C₃N₄/SnCoS₄, although the S and Co XPS peaks are decreased, the Sn, O, C and N

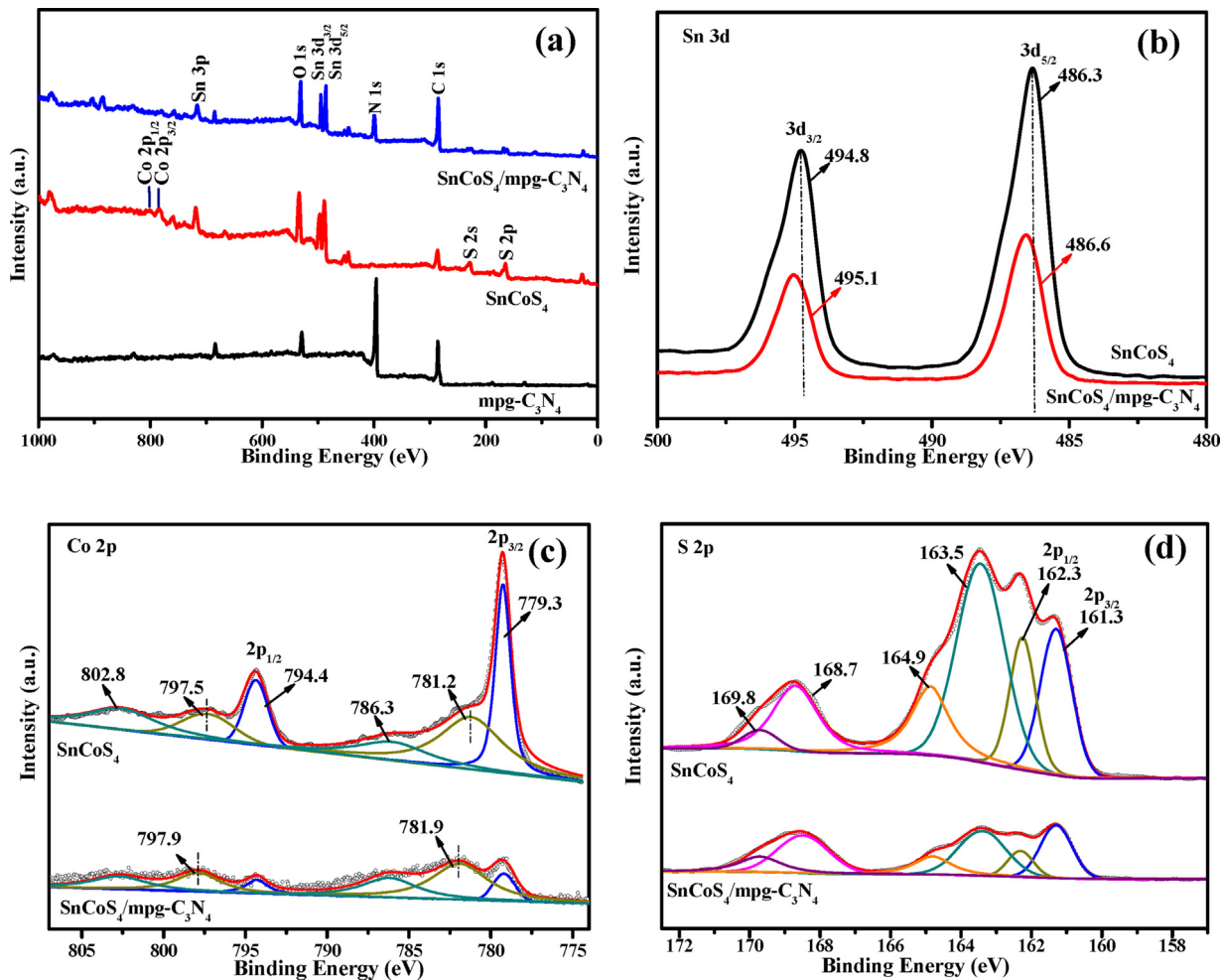


Fig. 7. (a) XPS survey spectrum of mpg-C₃N₄, SnCoS₄ and mpg-C₃N₄/SnCoS₄, high resolution XPS spectra of (b) Sn 3d (c) Co 2p and (d) S 2p obtained from SnCoS₄ and mpg-C₃N₄/SnCoS₄.

peaks can be observed clearly. Fig. 7b shows the XPS peaks at binding energies of 486.3 and 494.8 eV corresponding to the Sn 3d_{5/2} and Sn 3d_{3/2} for SnCoS₄, respectively, which can be assigned to the Sn⁴⁺ [39]. The binding energies of Sn 3d for mpg-C₃N₄/SnCoS₄ are shifted to the higher position at 486.6 and 495.1 eV compared with that of SnCoS₄, indicating that the valence of Sn⁴⁺ becomes lower due to the charge transfer between the mpg-C₃N₄/SnCoS₄. Therefore, it can be seen that there exists the strong interaction in heterojunction structure between unoccupied 3d orbitals of Sn and lone electron pair of mpg-C₃N₄ [34]. Besides, the spectrum of Sn shows a large full width a half maximum (FWHM) for mpg-C₃N₄/SnCoS₄, which results from the increased disorder and chemical inhomogeneity because of the smaller SnCoS₄ nanoparticle, suggesting the mpg-C₃N₄ with the high surface area can effectively stabilize the SnCoS₄ nanoparticle and prevent aggregation [40]. From Fig. 7c, the Co 2p XPS spectrum of SnCoS₄ exhibits two main peaks, including a Co 2p_{1/2} at 794.4 eV and a Co 2p_{3/2} at 779.3 eV. The secondary peaks at 779.3, 781.2 and 794.4 eV confirm the existence of a Co-S bond in the SnCoS₄, and the peak at 786.3 eV is attributed to the surface-adsorbed hydroxide species [41]. Meanwhile two broad peaks observed at 797.5 and 802.8 eV belong to cobalt salts. For mpg-C₃N₄/SnCoS₄, the secondary peaks at 781.9 and 797.9 are shift to higher binding energy in comparison with pristine SnCoS₄, which are similar to the shift of Sn peaks. The broad peaks of the S 2p indicate that there exists more than one chemical state of the sulfur element, which are deconvoluted into six peaks in Fig. 7d.

The peaks at 161.3 and 162.3 eV are related to the S 2p_{3/2} and S 2p_{1/2}, due to the presence of S²⁻ adsorbed on the surface, while the peaks at 163.5 eV belong to the bridging disulfides S₂²⁻ ligand [42]. The peak at 164.9 eV corresponds to the polymeric S_n²⁻, and the peaks at 168.7 and 169.8 eV can be assigned to SO₃²⁻ and SO₄²⁻, respectively [43]. Similar to the results of Sn and Co, the FWHM obviously broadens for mpg-C₃N₄/SnCoS₄, which also confirms the small particle size of SnCoS₄.

To understand the optical property of photocatalyst, the UV-vis diffuse reflectance spectra (UV-vis DRS) and photoluminescence (PL) spectra are conducted to study the effect of metal sulfide on the mpg-C₃N₄. As shown in Fig. 8a, the pristine mpg-C₃N₄ sample shows a good absorption edge at around 430 nm, and the band-gap value is estimated to be 2.65 eV by Tauc plot (Fig. S4) which is slightly decreased compared with the band-gap value of typical g-C₃N₄ at 2.7 eV [44]. It is found that the absorption edge of SnCoS₄ sample is less than 530 nm, and the band-gap value is determined to be 2.08 eV. The mpg-C₃N₄/SnCoS₄ demonstrates much broader absorption edge in the entire visible light region, and presents excellent and enhanced visible light absorption property compared with pristine SnCoS₄ and mpg-C₃N₄, resulting from the successful creation of heterojunction between mpg-C₃N₄ and SnCoS₄ [45–47]. Since CoS₂ possesses a narrow band gap [48], the absorption edge of mpg-C₃N₄/SnCoS₄ is in between that of mpg-C₃N₄/CoS₂ and mpg-C₃N₄/SnS₂.

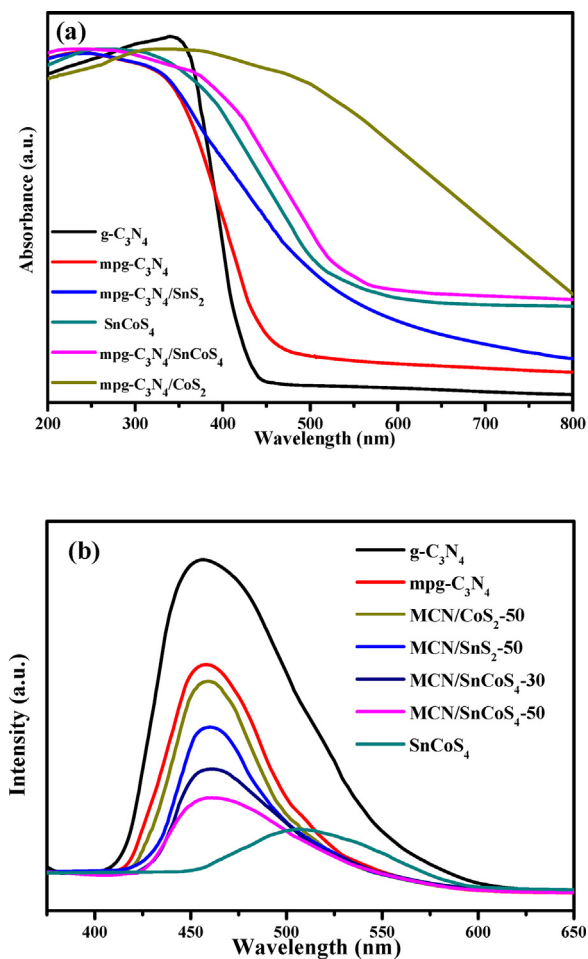


Fig. 8. (a) UV-vis diffuse reflectance spectra of g-C₃N₄, mpg-C₃N₄, SnCoS₄, mpg-C₃N₄/SnCoS₄, mpg-C₃N₄/CoS₂ and mpg-C₃N₄/SnS₂, (b) Photoluminescence spectra of g-C₃N₄, mpg-C₃N₄, SnCoS₄, MCN/CoS₂-50, MCN/SnS₂-50, MCN/SnCoS₄-30 and mpg-C₃N₄/SnCoS₄-50.

Fig. 8b shows the PL spectra of as-prepared samples under the excitation wavelength of 360 nm. In general, the recombination of photogenerated electron-hole pairs can release energy to form the PL emission, and the lower PL intensity shows the lower recombination of photogenerated charge carrier, which leads to higher photocatalytic activity. The g-C₃N₄ has a strong emission peak at around 455 nm, corresponding to the UV-vis results. The emission intensity of mpg-C₃N₄ sample is lower than that of pristine g-C₃N₄ at the similar emission position, indicating that electron-pairs recombination of mpg-C₃N₄ is efficiently inhibited. The pristine SnCoS₄ has the PL emission peak at round 520 nm, and the PL intensity of pristine SnCoS₄ is rather low because the amount of the photo-induced electron-hole pairs is much less than that of g-C₃N₄ or mpg-C₃N₄ under the same irradiation condition, which consists with the results of previous literature [49]. The PL emission of mpg-C₃N₄/SnCoS₄ is significantly quenched in comparison with the pristine mpg-C₃N₄, MCN/CoS₂ and MCN/SnS₂, demonstrating the composite has the low rate of electron-pairs recombination. It is remarkable that in the case of mpg-C₃N₄/SnCoS₄, the enhanced charge transfer capability at the interface of heterostructure can result in the superior photocatalytic activity.

3.2. Photocatalytic activity evaluation

The photocatalytic activity of as-prepared samples was evaluated by MB and RhB degradation under the visible-light irradiation.

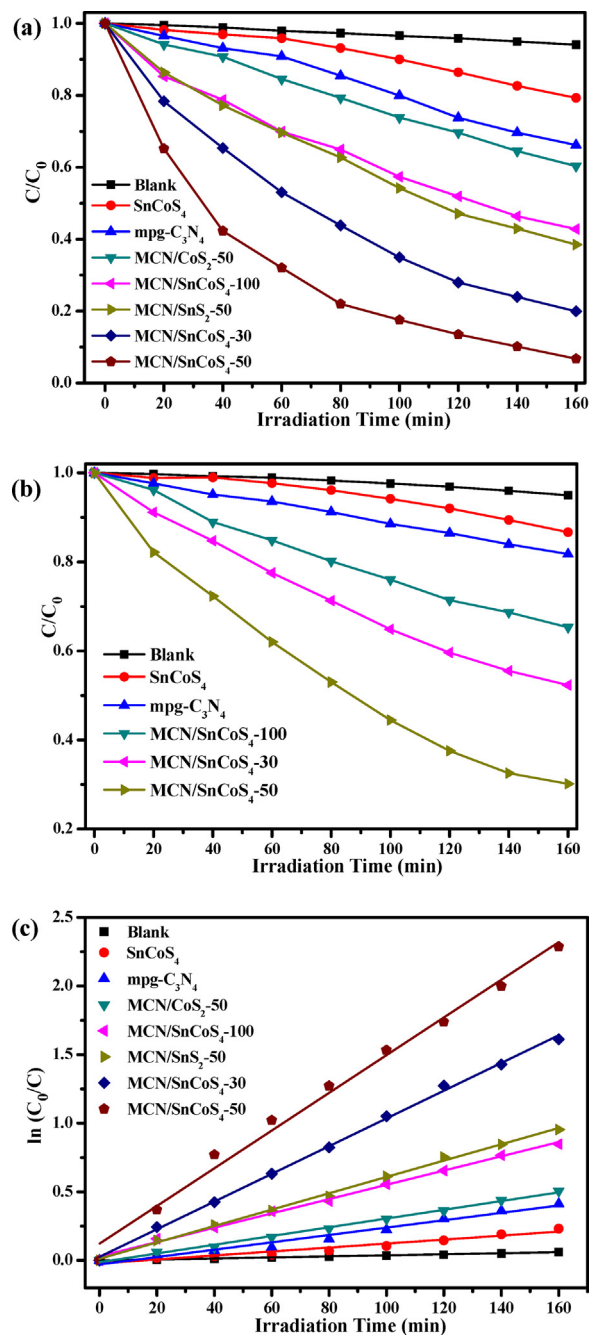


Fig. 9. Photocatalytic degradation efficiencies of (a) MB and (b) RhB over the as-prepared samples under visible-light irradiation, (c) the first-order kinetics of MB photocatalytic degradation.

The degradation efficiency of MB is only reduced to 20% and 34% for the pristine mpg-C₃N₄ and SnCoS₄, respectively (Fig. 9a), and that of RhB is decreased to 13% and 18%, respectively (Fig. 9b). For the mpg-C₃N₄/metal sulfide composites, MCN/SnCoS₄-50 exhibits the superior degradation efficiency of MB (95%) and the good removal efficiency of RhB (70%). The degradation efficiencies of MB are in the order of SnCoS₄ < mpg-C₃N₄ < MCN/CoS₂-50 < MCN/SnCoS₄-100 < MCN/SnS₂-50 < MCN/SnCoS₄-30 < MCN/SnCoS₄-50. The MCN/SnCoS₄-50 shows the highest reaction rate constant (0.01374 min^{-1}) which is 9.48, 5.11, 4.32, 2.64, 2.31 and 1.36 times higher than SnCoS₄ (0.00145 min^{-1}), mpg-C₃N₄ (0.00269 min^{-1}), MCN/CoS₂-50 (0.00318 min^{-1}), MCN/SnCoS₄-100 (0.00521 min^{-1}), MCN/SnS₂-50 (0.00596 min^{-1}) and

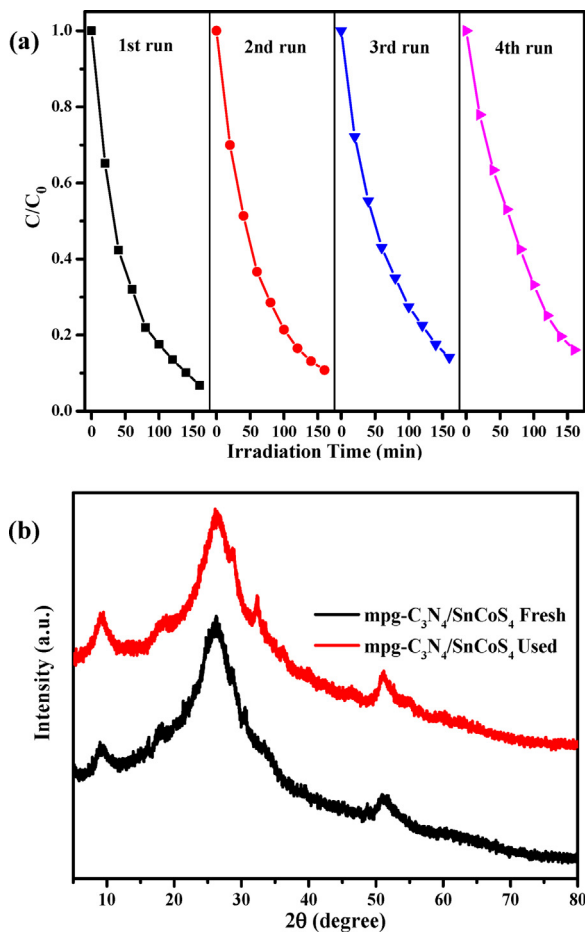


Fig. 10. (a) Photocatalytic recycle degradation of MB using mpg-C₃N₄/SnCoS₄, (b) XRD patterns of mpg-C₃N₄/SnCoS₄ before and after the recycle experiment.

MCN/SnCoS₄-30 (0.0101 min⁻¹), respectively. Besides, the degradation efficiency of RhB over MCN/SnCoS₄ composites is higher and more prominent than pristine mpg-C₃N₄ or SnCoS₄ under the same experimental conditions. Therefore, it could be deduced from the above results that the photocatalytic activity of binary metal sulfides (MCN/SnCoS₄) heterojunction is superior to that of single metal sulfide such as MCN/CoS₂ and MCN/SnS₂, since coexisting Sn⁴⁺ and Co⁴⁺ can affect mpg-C₃N₄ to form more stable and efficient charge transfer system [50]. Moreover, the SnCoS₄ content can influence the photocatalytic activity of MCN/SnCoS₄ composite.

The photostability of MCN/SnCoS₄ composite was further carried out by recycling the photocatalyst for four times in Fig. 10a. There is no obvious decreased during the photocatalytic degradation of MB after four degradation-regeneration runs. About 85% MB can be degraded over MCN/SnCoS₄-50 after four cycles. The corresponding XRD pattern of MCN/SnCoS₄-50 employed in the recycle tests (Fig. 10b) shows that there is no obvious different from the intact sample, demonstrating that MCN/SnCoS₄ has superior stability and recyclability.

3.3. Photocatalytic mechanism

The photocatalytic mechanism of the mpg-C₃N₄/SnCoS₄ composite was investigated by determining the main active species of h⁺, •O₂⁻ and •OH during the photocatalytic degradation. Scavengers (EDTA, BQ and IPA) were separately added to trap h⁺, •O₂⁻ and •OH. As shown in Fig. 11, the photocatalytic efficiency significantly decreases with addition of BQ, and the addition of EDTA can

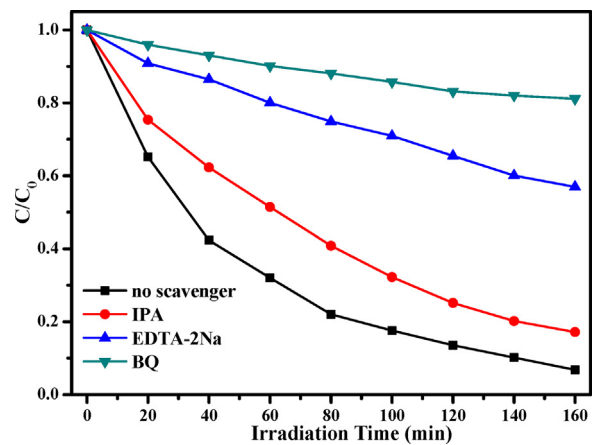


Fig. 11. Effects of different scavengers on the degradation of MB in the presence of mpg-C₃N₄/SnCoS₄ under visible-light irradiation.

partially suppress the photocatalytic activity, suggesting that •O₂⁻ and h⁺ should be the main active species in this decomposition process. However, there is no significant decrease in the degradation rate of MB in the presence of IPA, showing that •OH is not an important contributor to the degradation process.

Mott-Schottky (M-S) plots can be used to determine both donor density and flat band potential of semiconductor. As shown in Fig. 12a, the positive slopes indicate the typical n-type characteristics for SnCoS₄, mpg-C₃N₄ and mpg-C₃N₄/SnCoS₄ [51]. For the property of n-type semiconductor, the flat band potential determined from M-S plots is very close to the conduction band (CB) of semiconductor [52]. Based on the intersection, the flat band potentials are approximately -1.38 V, -1.02 V and -0.96 V for SnCoS₄, mpg-C₃N₄ and mpg-C₃N₄/SnCoS₄, respectively. Besides, the slope of mpg-C₃N₄/SnCoS₄ is lower than that of pristine mpg-C₃N₄ and SnCoS₄, indicating that the composite has the higher carrier concentration, and the enhanced donor density could effectively improve the transfer of electron-hole between mpg-C₃N₄ and SnCoS₄. The CB potential obtained from M-S plots together with the band gaps estimated from UV-vis absorption spectra can present absolute energy scheme as shown in Fig. 12b. Compared with pristine mpg-C₃N₄, the mpg-C₃N₄/SnCoS₄ heterostructure not only narrows the band gap but also changes the CB and VB position. The CB potential of mpg-C₃N₄/SnCoS₄ (-0.96 V vs. Ag/AgCl, pH 5.6) is more negative than that of O₂/•O₂⁻ (-0.13 V vs. Ag/AgCl), while the VB potential of mpg-C₃N₄/SnCoS₄ (+1.07 V vs. Ag/AgCl) is not more positive than the potential of •OH/OH⁻ (+2.19 V vs. Ag/AgCl) [24,53]. Therefore, the electrons on the CB potential of the composite can react with O₂ to form •O₂⁻, but the holes are difficult to oxidize OH⁻/H₂O to produce active species •OH in the photocatalytic reaction. This indicates that main active species •O₂⁻ are directly formed during the degradation process, which is consistent with the result of scavengers trapping experiment.

Based on the above analysis, the superior photocatalytic activity of mpg-C₃N₄/SnCoS₄ can be attributed to its interior electrical structure as well as porous morphology [54–56]. Due to the interface effect between the mpg-C₃N₄ and SnCoS₄, the excited electrons on the CB of SnCoS₄ can be transferred to that of mpg-C₃N₄, and the holes produced by mpg-C₃N₄ are injected into the VB of SnCoS₄, resulting in the effective separation of photogenerated electrons and holes, as shown in Scheme 2. The electrons on the mpg-C₃N₄ further react with dissolved oxygen molecules to form main active species •O₂⁻, while the holes diffused to the surface of SnCoS₄ act as the active species for the degradation process. As a result, the incorporation of binary metal sulfides into mpg-C₃N₄ to form the n-n heterojunction structure can extend the

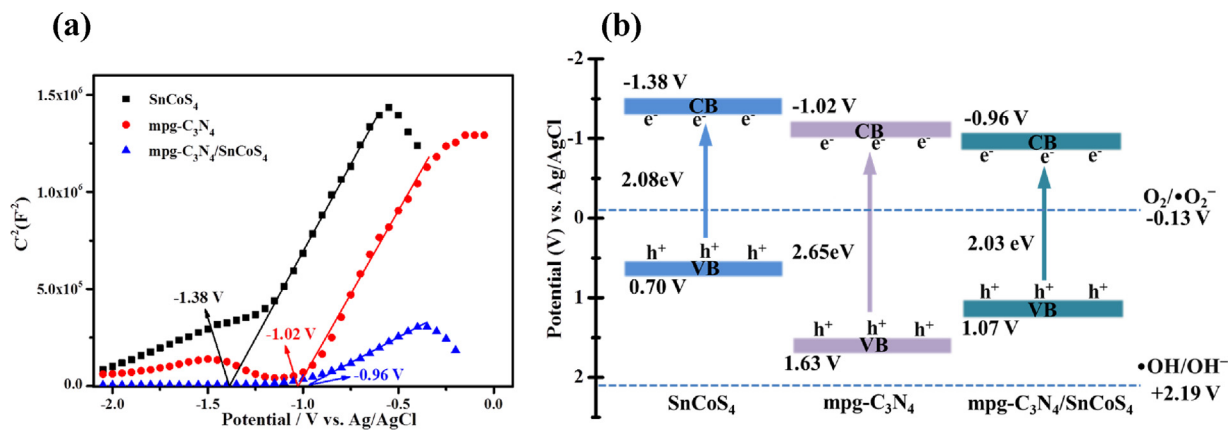
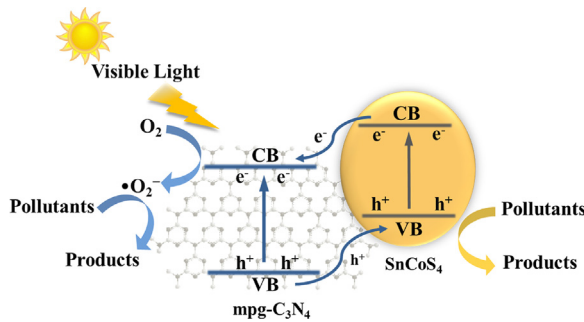


Fig. 12. (a) Electrochemical Mott-Schottky plots of mpg-C₃N₄, SnCoS₄ and mpg-C₃N₄/SnCoS₄, (b) electronic band structure of mpg-C₃N₄, SnCoS₄ and mpg-C₃N₄/SnCoS₄.



Scheme 2. Schematic of photocatalytic degradation over the mpg-C₃N₄/SnCoS₄ under visible light irradiation.

visible light absorption range, narrow the band gap, alter the CB and VB potential and suppress recombination probability of charge carrier. Secondly, mpg-C₃N₄/SnCoS₄ heterojunction with high surface area can provide more catalytic active sites and produce multiple reflection effect within the interior cavity under the visible light irradiation. Due to the *in-situ* synthesis of SnCoS₄, mpg-C₃N₄ as a porous substrate can restrict the growth of SnCoS₄ and offer a better contact interface. Therefore, the formation of the n-n heterojunction and high surface area can be considered as the primary factor for the enhanced photocatalytic activity.

4. Conclusion

In summary, the novel mpg-C₃N₄/SnCoS₄ photocatalysts were successfully synthesized *via* a facile *in situ* hydrothermal method and the photocatalytic degradation of organic pollution including RhB and MB was investigated under visible irradiation. MCN/SnCoS₄-50 composite exhibited the highest degradation efficiency of MB (95%) compared to pristine SnCoS₄, mpg-C₃N₄, MCN/CoS₂-50 as well as MCN/SnS₂-50. Meanwhile, the composite can effectively remove the RhB (70%), and the photocatalytic activity of mpg-C₃N₄/SnCoS₄ was influenced by mpg-C₃N₄ content. Moreover, the prepared photocatalysts showed the excellent stability under visible light irradiation. The enhanced photocatalytic activity and stability of mpg-C₃N₄/SnCoS₄ can be ascribed to the large surface area of mesoporous structure, formation of n-n type heterojunction, inhibited electron-hole recombination and the intimate synergistic interactions. The conduction band potential of mpg-C₃N₄/SnCoS₄ (-0.96 V vs. Ag/AgCl) is more negative than the potential of O₂/•O₂⁻ (-0.13 V), and trapping tests demonstrate that superoxide radical anions play the major role in the degradation process. The results here demonstrate a facile preparation method

for fabricating efficient visible-light-driven heterojunction photocatalysts for environmental remediation.

Acknowledgement

This work was supported by the Natural Science Foundation of Jiangsu Province (Nos. BK20150259, BK20160277).

Appendix A. Supplementary data

Supplementary data associated with this article can be found, in the online version, at <http://dx.doi.org/10.1016/j.apcatb.2017.07.003>.

References

- [1] C.C. Chen, W.H. Ma, J.C. Zhao, Chem. Soc. Rev. 39 (2010) 4206–4219.
- [2] F.K. Meng, J.T. Li, S.K. Cushing, M.J. Zhi, N.Q. Wu, J. Am. Chem. Soc. 135 (2013) 10286–10289.
- [3] W. Chen, Y.X. Hua, Y. Wang, T. Huang, T.Y. Liu, X.H. Liu, J. Catal. 349 (2017) 8–18.
- [4] Y.J. Yuan, D.Q. Chen, X.F. Shi, J.R. Tu, B. Hu, L.X. Yang, Z.T. Yu, Z.G. Zou, J. Chem. Eng. 313 (2017) 1438–1446.
- [5] M.S. Faber, M.A. Lukowski, Q. Ding, N.S. Kaiser, S. Jin, J. Phys. Chem. C 118 (2014) 21347–21356.
- [6] H.A. Sorkhabi, B.R. Moghadam, E. Asghari, R. Bagheri, Z. Hosseinpour, J. Chem. Eng. 308 (2017) 275–288.
- [7] X.L. Yu, A. Shavel, X.Q. An, Z.S. Luo, M. Ibáñez, A. Cabot, J. Am. Chem. Soc. 136 (2014) 9236–9239.
- [8] X. Zhang, P. Zhang, L.J. Wang, H.Q. Gao, J.T. Zhao, C.H. Liang, J.H. Hu, G.S. Shao, Appl. Catal. B 192 (2016) 17–25.
- [9] A.J. Biacchi, D.D. Vaughn, R.E. Schaak, J. Am. Chem. Soc. 135 (2013) 11634–11644.
- [10] L.Q. Ye, C.Q. Han, Z.Y. Ma, Y.M. Leng, J. Li, X.X. Ji, D.Q. Bi, H.Q. Xie, Z.X. Huang, J. Chem. Eng. 307 (2017) 311–318.
- [11] K. Li, R. Chen, S.L. Li, S.L. Xie, L.Z. Dong, Z.H. Kang, J.C. Bao, Y.Q. Lan, ACS Appl. Mater. Interfaces 8 (2016) 14535–14541.
- [12] J.G. Yu, J. Zhang, M. Jaroniec, Green. Chem. 12 (2010) 1611–1614.
- [13] J.B. Ye, T. Chen, Q.N. Chen, W.X. Chen, Z.T. Yu, S.R. Xu, J. Mater. Chem. A 4 (2016) 13194–13202.
- [14] W.J. Ong, L.L. Tan, Y.H. Ng, S.T. Yong, S.P. Chai, Chem. Rev. 116 (2016) 7159–7329.
- [15] Z.F. Jiang, K. Qian, C.Z. Zhu, H.L. Sun, W.M. Wan, J.M. Xie, H.M. Li, P.K. Wong, S.Q. Yuan, Appl. Catal. B 210 (2017) 194–204.
- [16] R. Kuriki, K. Sekizawa, O. Ishitani, K. Maeda, Angew. Chem. Int. Ed. 54 (2015) 2406–2409.
- [17] C. Ye, X.Z. Wang, J.X. Li, Z.J. Li, X.B. Li, L.P. Zhang, B. Chen, C.H. Tung, L.Z. Wu, ACS Catal. 6 (2016) 8336–8341.
- [18] J.H. Liu, S.Y. Xie, Z.B. Geng, K.K. Huang, L. Fan, W.L. Zhou, L.X. Qiu, D.L. Gao, L. Ji, L.M. Duan, L.H. Lu, W.F. Li, S.Z. Bai, Z.R. Liu, W. Chen, S.H. Feng, Y.G. Zhang, Nano Lett. 16 (2016) 6568–6575.
- [19] Q.L. Xu, B. Cheng, J.G. Yu, G. Liu, Carbon 118 (2017) 241–249.
- [20] Y. Shiraishi, Y. Kofuji, H. Sakamoto, S. Tanaka, S. Ichikawa, T. Hirai, ACS Catal. 5 (2015) 3058–3066.
- [21] K. Schwinghammer, M.B. Mesch, V. Duppel, C. Ziegler, J. Senker, B.V. Lotsch, J. Am. Chem. Soc. 136 (2014) 1730–1733.

[22] J.R. Ran, T.Y. Ma, G.P. Gao, X.W. Du, S.Z. Qiao, *Energy Environ. Sci.* 8 (2015) 3708–3717.

[23] G.H. Dong, D. Chen, J.M. Luo, Y.Q. Zhu, Y.B. Zeng, C.Y. Wang, *J. Hazard. Mater.* 335 (2017) 66–74.

[24] P.X. Qiu, C.M. Xu, H. Chen, F. Jiang, X. Wang, R.F. Lu, X.R. Zhang, *Appl. Catal. B* 206 (2017) 319–327.

[25] L.C. Jia, H.Q. Wang, D. Dhawale, C. Anand, M.A. Wahab, Q.M. Ji, K. Ariga, A. Vinu, *Chem. Commun.* 50 (2014) 5976–5979.

[26] Y. Wang, J. Yao, H.R. Li, D.S. Su, M. Antonietti, *J. Am. Chem. Soc.* 133 (2011) 2362–2365.

[27] Y.T. Gong, P.F. Zhang, X. Xu, Y. Li, H.R. Li, Y. Wang, *J. Catal.* 297 (2013) 272–280.

[28] X.C. Wang, K. Maeda, X.F. Chen, K. Takanabe, K. Domen, Y.D. Hou, X.Z. Fu, M. Antonietti, *J. Am. Chem. Soc.* 131 (2009) 1680–1681.

[29] A. Indra, A. Acharjya, P.W. Menezes, C. Merschjann, D. Hollmann, M. Schwarze, M. Aktas, A. Friedrich, S. Lochbrunner, A. Thomas, M. Driess, *Angew. Chem. Int. Ed.* 56 (2017) 1653–1657.

[30] J. Xu, T. Chen, J.K. Shang, K.Z. Long, Y.X. Li, *Microporous Microporous Mater.* 211 (2015) 105–112.

[31] K.Ting Lee, Y.C. Liang, H.H. Lin, C.H. Li, S.Y. Lu, *Electrochim. Acta* 219 (2016) 241–250.

[32] Q. Liang, M. Zhang, C.H. Liu, S. Xu, Z.Y. Li, *Appl. Catal. A* 519 (2016) 107–115.

[33] J. Xu, Y. Wang, J.K. Shang, Q. Jiang, Y.X. Li, *Catal. Sci. Technol.* 6 (2016) 4192–4200.

[34] Y.Q. Zhang, Z.L. Ma, D.D. Liu, S. Dou, J.M. Ma, M. Zhang, Z.P. Guo, R. Chen, S.Y. Wang, *J. Mater. Chem. A* 5 (2017) 512–518.

[35] Z.K. Zhao, W.Z. Li, Y.T. Dai, G.F. Ge, X.W. Guo, G.R. Wang, *ACS Sustainable Chem. Eng.* 3 (2015) 3355–3364.

[36] S.H. Shen, D.M. Zhao, J. Chen, L.J. Guo, S.S. Mao, *Appl. Catal. A* 521 (2016) 111–117.

[37] Z.K. Zhao, Y.T. Dai, J.H. Lin, G.R. Wang, *Chem. Mater.* 26 (2014) 3151–3161.

[38] S.K. Le, T.S. Jiang, Y.W. Li, Q. Zhao, Y.Y. Li, W.B. Fang, M. Gong, *Appl. Catal. B* 200 (2017) 601–610.

[39] Y.C. Zhang, F. Zhang, Z.J. Yang, H.G. Xue, D.D. Dionysiou, *J. Catal.* 344 (2016) 692–700.

[40] C.H. Liu, B.H. Mao, J. Gao, S. Zhang, X. Gao, Z. Liu, S.T. Lee, X.H. Sun, S.D. Wang, *Carbon* 50 (2012) 3008–3014.

[41] P. Ganesan, M. Prabu, J. Sanetuntikul, S. Shanmugam, *ACS Catal.* 5 (2015) 3625–3637.

[42] Y.Y. Yang, F. Li, W.Z. Li, W.B. Gao, H. Wen, J. Li, Y.P. Hu, Y.T. Luo, R. Li, *Int. J. Hydrogen Energy* 42 (2017) 6665–6673.

[43] Y.Ru Liu, X. Shang, W.K. Gao, B. Dong, J.Q. Chi, X. Li, K.L. Yan, Y.M. Chai, Y.Q. Liu, C.G. Liu, *Appl. Surf. Sci.* 412 (2017) 138–145.

[44] B. Lin, G.D. Yang, B.L. Yang, Y.X. Zhao, *Appl. Catal. B* 198 (2016) 276–285.

[45] Y. Huang, Y.L. Liang, Y.F. Rao, D.D. Zhu, J.J. Cao, Z.X. Shen, W.K. Ho, S.C. Lee, *Environ. Sci. Technol.* 51 (2017) 2924–2933.

[46] Z.Y. Wang, Y. Huang, W.K. Ho, J.J. Cao, Z.X. Shen, S.C. Lee, *Appl. Catal. B* 199 (2016) 123–133.

[47] Q. Zhang, Y. Huang, S.Q. Peng, Y.F. Zhang, Z.X. Shen, J.J. Cao, W.K. Ho, S.C. Lee, D.Y. Pui, *Appl. Catal. B* 204 (2017) 346–357.

[48] L. Zhu, S.B. Jo, S. Ye, K. Ullah, Z.D. Meng, W.C.n Oh, *J. Ind. Eng. Chem.* 22 (2015) 264–271.

[49] M. Wang, M. Shen, L.X. Zhang, J.J. Tian, X.X. Jin, Y.J. Zhou, J.L. Shi, *Carbon* 120 (2017) 23–31.

[50] F. Chen, Q. Yang, Y.L. Wang, J.W. Zhao, D.B. Wang, X.M. Li, Z. Guo, H. Wang, Y.C. Deng, C.G. Niu, G.M. Zeng, *Appl. Catal. B* 205 (2017) 133–147.

[51] T. Giannakopoulou, I. Papailias, N. Todorova, N. Boukos, Y. Liu, J.G. Yu, C. Trapalis, *J. Chem. Eng.* 310 (2017) 571–580.

[52] L. Zhou, H.Y. Zhang, H.Q. Sun, S.M. Liu, M.O. Tade, S.B. Wang, W.Q. Jin, *Catal. Sci. Technol.* 6 (2016) 7002–7023.

[53] F.F. Wu, M.L. Lv, X.Q. Sun, Y.H. Xie, H.M. Chen, S. Ni, G. Liu, X.X. Xu, *ChemCatChem* 8 (2016) 615–623.

[54] B. Lin, H. An, X.Q. Yan, T.X. Zhang, J.J. Wei, G.D. Yang, *Appl. Catal. B* 210 (2017) 173–183.

[55] B. Lin, S. Chen, F. Dong, G.D. Yang, *Nanoscale* 9 (2017) 5273–5279.

[56] C. Xue, T.X. Zhang, S.J. Ding, J.J. Wei, G.D. Yang, *ACS Appl. Mater. Interfaces* 9 (2017) 16091–16102.